Mirabbos Hojamberdiev, J. Manuel Mora-Hernandez, Ronald Vargas, Akira Yamakata, Kunio Yubuta, Eva Maria Heppke, Leticia M. Torres-Martínez, Katsuya Teshima, Martin Lerch

Time-retrenched synthesis of BaTaO2N by localizing an NH3 delivery system for visible-light-driven photoelectrochemical water oxidation at neutral pH: Solid-state reaction or flux method?

Citation details
Hojamberdiev, M., Mora-Hernandez, J. M., Vargas, R., Yamakata, A., Yubuta, K., Heppke, E. M., Torres-Martínez, L. M., Teshima, K. Lerch, M. (2021). Time-Retrenched Synthesis of BaTaO2N by Localizing an NH3 Delivery System for Visible-Light-Driven Photoelectrochemical Water Oxidation at Neutral pH: Solid-State Reaction or Flux Method? ACS Applied Energy Materials, 4(9), 9315–9327. https://doi.org/10.1021/acsaem.1c01539.

Time-retrenched synthesis of $BaTaO_2N$ by localizing an NH_3 delivery system for visible-light-driven photoelectrochemical water oxidation at neutral pH: Solid-state reaction or flux method?

Mirabbos Hojamberdiev[1,*], J. Manuel Mora-Hernandez[2], Ronald Vargas[3], Akira Yamakata[4], Kunio Yubuta[5,6], Eva Maria Heppke[1], Leticia M. Torres-Martínez[7,8], Katsuya Teshima[9,10] and Martin Lerch[1]

[1]*Institut für Chemie, Technische Universität Berlin, Straße des 17. Juni 135, 10623 Berlin, Germany*

[2]*CONACYT - Universidad Autónoma de Nuevo León, Facultad de Ingeniería Civil, Departamento de Ecomateriales y Energía, Av. Universidad S/N Ciudad Universitaria, San Nicolás de los Garza, Nuevo León, C.P. 66455, Mexico*

[3]*Instituto Tecnológico de Chascomús (INTECH). Universidad Nacional de San Martín (UNSAM). Consejo Nacional de Investigaciones Científicas y Técnicas (CONICET). Avenida Intendente Marino, Km 8,2, (B7130IWA), Chascomús, Provincia de Buenos Aires, Argentina*

[4]*Graduate School of Engineering, Toyota Technological Institute, 2-12-1 Hisakata, Tempaku-ku, Nagoya 468-8511, Japan*

[5]*Institute for Materials Research, Tohoku University, 2-1-1 Katahira, Aoba-ku, Sendai 980-8577, Japan*

[6]*Department of Applied Quantum Physics and Nuclear Engineering, Kyushu University, Fukuoka 819-0395, Japan*

[7]*Universidad Autónoma de Nuevo León, Facultad de Ingeniería Civil, Departamento de Ecomateriales y Energía, Av. Universidad S/N Ciudad Universitaria, San Nicolás de los Garza, Nuevo León, C.P. 66455, Mexico*

[8]*Centro de Investigación en Materiales Avanzados, S.C. (CIMAV), Miguel de Cervantes No. 120. Complejo Ind. Chihuahua, Chihuahua, Chih, C.P. 31136, Mexico*

[9]*Research Initiative for Supra-Materials, Shinshu University, 4-17-1 Wakasato, Nagano 380-8553, Japan*

[10]*Department of Materials Chemistry, Shinshu University, 4-17-1 Wakasato, Nagano 380-8553, Japan*

*Corresponding author: E-mail: khujamberdiev@tu-berlin.de, hmirabbos@gmail.com

ABSTRACT:

Among 600 nm-class transition metal oxynitrides, $BaTaO_2N$ with a cubic $Pm\bar{3}m$ perovskite-type structure is promising for solar water oxidation due to its absorption of visible light up to 660 nm, narrower bandgap (E_g= 1.9 eV), appropriate valence band edge position for oxygen evolution, good stability in concentrated alkaline solutions, and nontoxicity. However, high defect density stemmed from long high-temperature ammonolysis limits the separation and transfer efficiency of photogenerated charge carriers in $BaTaO_2N$. Here, an NH_3 delivery system is specifically localized just above the synthesis mixture to reduce the synthesis time and defect density of $BaTaO_2N$ by a fresh supply of more active nitriding species and minimizing the generation of N_2 and H_2. Particularly, the effects of synthesis temperature (700-950°C), synthesis time (1-8 h), and gas composition are systematically investigated to gain insights into the formation of single-phase $BaTaO_2N$ by solid-state reaction and flux method. Time-dependent experiments conducted at 950°C show that single-phase $BaTaO_2N$ can be synthesized ≥6 h and ≥4 h by solid-state reaction and flux method, respectively, revealing the advantage of flux method over solid-state reaction in a localized NH_3 delivery system. Subsequently, the separation and transfer efficiency and kinetics of photogenerated charge carriers are studied in $BaTaO_2N$ samples. Photoelectrochemical studies made it possible to resolve trends during visible-light-induced water oxidation, evidencing the inverse relationship between recombination and charge transfer phenomena. Transient absorption spectroscopy reveals that the dynamics of the photogenerated charge carriers in both types of $BaTaO_2N$ samples are different: (i) $BaTaO_2N$ synthesized by flux method has a greater number of holes despite the similar number of deeply trapped charge carriers and (ii) solid-state reaction led to the formation of a higher number of free electrons in $BaTaO_2N$. The findings demonstrate the advantage of reducing the transfer distance of active nitriding species to the surface of the synthesis mixture for enhancing the photoelectrochemical water oxidation of $BaTaO_2N$ at neutral pH.

KEYWORDS: $BaTaO_2N$; Ammonolysis; Flux method; Solid-state reaction; Charge carrier dynamics; Photoelectrochemical performance

1. INTRODUCTION

Sunlight-driven splitting of water is a potential chemical technique to directly generating green hydrogen due to its environmental friendliness, cost-competitiveness, and technological simplicity.[1-4] However, to attain large-scale commercialization, photoelectrochemical water splitting requires a solar-to-hydrogen (STH) energy conversion efficiency of more than 10%.[5] In comparison to the two-electron transfer reaction ($2H^+ + 2e^- \rightarrow H_2$) for molecular hydrogen evolution,[6] the sluggish kinetics of the four-electron transfer reaction ($4OH^- \rightarrow 4e^- + 2H_2O + O_2$) is still an obstacle for efficient evolution of molecular oxygen from sunlight-driven splitting of water.[7] Hence, it necessitates developing and applying novel strategies for accelerating the reaction kinetics for molecular oxygen evolution of various photocatalysts that function at longer wavelengths.

Among quaternary oxynitrides, $BaTaO_2N$ with a cubic $Pm\bar{3}m$ perovskite-type structure has been of significant interest because of its ability to absorb visible light (< 660 nm), narrower bandgap (E_g = 1.9 eV), sufficient valence band potential to drive the water oxidation reaction, good stability, and nontoxicity.[8] About 18 $mA \cdot cm^{-2}$ photocurrent was estimated to be yielded by $BaTaO_2N$ under AM 1.5G sunlight,[9] and its water splitting reaction can proceed without applying an external bias due to the sufficient valence band and conduction band potentials.[10,11]

Earlier, molecular hydrogen and oxygen were successfully generated from sunlight-driven water splitting over the $BaZrO_3$–$BaTaO_2N$ solid solution-based photoelectrochemical cell (1.0 V applied bias vs. Pt).[12] The onset potential of the $BaTaO_2N$ photoanode fabricated by an electrophoretic deposition followed by post-necking was successfully shifted towards more negative potentials for photoelectrochemical water splitting (0.7 V applied bias vs. Pt).[13] By applying a particle transfer technique and Co-cocatalyst modification, a 4.2 $mA \cdot cm^{-2}$ photocurrent was achieved for the $BaTaO_2N$ photoanode at 1.2 V vs. RHE under simulated sunlight.[9] Pihosh et al.[14] increased the photocurrent of $BaTaO_2N$ to ~4.5 $mA \cdot cm^{-2}$ at 1.2 V vs. RHE under simulated sunlight by creating a core-shell heterojunction with Ta_3N_5 nanorods and modifying with $FeNiO_x$ cocatalyst. Further, a 4.6 $mA \cdot cm^{-2}$ photocurrent was yielded for $BaTaO_2N$ upon

combination with Ta_2N/Ta and modification with CoO_x cocatalyst at 1.2 V vs. RHE, while a 9% IPCE (incident photon-to-current efficiency) at 600 nm was realized during simulated sunlight-driven water oxidation reaction.[15] Annealing of inactive as-synthesized $BaTaO_2N$ particles in Ar was found to be advantageous to maximize the photocurrent to 6.5 $mA \cdot cm^{-2}$ at 1.23 V vs. RHE, which showed a good stability over 24 h (79% initial photocurrent was retained).[16] Very recently, Castelli and coworkers[17] found that the theoretical overpotential of the TaO_2N-(100) surface of $BaTaO_2N$ can be effectively decreased to 0.37 V under (photo)electrochemical conditions by applying 1% tensile uniaxial strain. Considering all the above-mentioned advantages of $BaTaO_2N$ over other metal (oxy)nitrides, further studies are however indispensable to further enhance the efficiency and stability of $BaTaO_2N$ for the design and manufacturing of photoelectrochemical tandem cells to meet the prerequisites for overall water splitting.[18–20] In any case, the electrochemical properties are responsible for these effects, and it is important to study the trends in the conditions that will resolve the optoelectronic effects to understand and guide improvements.

In general, the preparation process of $BaTaO_2N$ includes an oxide precursor synthesis followed by nitridation at high temperature under a flow of gaseous NH_3 for an extended time,[21,22] generating various bulk and surface defects. Such defects are known to hinder a separation-transfer process of photoexcited electrons and holes due to a high recombination rate. In our previous works,[23,24] we have drastically reduced the synthesis time and defect density of $BaTaO_2N$ by applying a flux method assisted by an NH_3 flow, where NH_3 was supplied via flowing it from one end to the other of the horizontal tube (Figure S1a). In such system, the transfer distance of active nitriding species (NH_2, NH, N, etc.) becomes too far from a synthesis mixture even at a high gas flow rate, maximizing the generation of N_2 and H_2 before active nitriding species reach the surface of the synthesis mixture. Consequently, an insufficient supply of active nitriding species leads to higher defect density in $BaTaO_2N$ due to a prolonged high-temperature ammonolysis. In this study, we specifically localize an NH_3 delivery system (Figure S1b) just above the synthesis mixture using a small-diameter gas-supplying horizontal tube to reduce the defect density of

$BaTaO_2N$, which is generally resulted from long high-temperature ammonolysis, by a fresh supply of more active nitriding species. Here, the effects of synthesis temperature (700-950°C), synthesis time (1-8 h), and gas composition on the solid-state and flux synthesis of single-phase $BaTaO_2N$ are systematically investigated. Subsequently, the separation-transfer efficiency and kinetics of photo-induced electrons and holes of the solid-state- and flux-synthesized $BaTaO_2N$ samples are studied.

2. EXPERIMENTAL

2.1. Synthesis

In this study, solid-state reaction and flux method were applied to synthesize $BaTaO_2N$ (Figures S2a and S2b). For the solid-state reaction, $BaCO_3$ (>99%, Fluka) and Ta_2O_5 (99%, Alfa Aesar) were mixed, and KCl (>99.5% Fluka) was introduced as a flux to the above mixture (50 mol% solute concentration) for the flux method. The well-homogenized mixture in a platinum crucible was placed just under the localized NH_3 delivery system, heated at 700-950°C (a heating rate of 500°C·h^{-1}) for 2-8 h in NH_3 atmosphere (12.5 L·h^{-1}, ≥99,95 %, Air Liquide), and cooled naturally in a horizontal tube furnace (Carbolite Gero) using a SiO_2-tube. Afterward, the resulting samples were collected, washed with dilute nitric acid and water and dried at 70°C for 10 h. The $BaTaO_2N$ samples synthesized by solid-state reaction and flux method were indicated as BTON-S and BTON-F, respectively. The BTON-S and BTON-F samples were also subjected to annealing at 700°C for 1 h in Ar atmosphere to reduce the negative effect of surface defects on photoelectrochemical performance[16] and labeled as BTON-S(Ar) and BTON-F(Ar), respectively. The details of characterization methods and photoelectrochemical measurements are given in Supporting Information.

3. RESULTS AND DISCUSSION

Various synthesis parameters, such as synthesis temperature, synthesis time, gas composition, gas flow rate, etc., significantly influence the phase purity, crystallinity, and morphology of transition metal oxynitrides. Thus, by localizing an NH_3 delivery system right above the synthesis mixture, the effects of

synthesis temperature (700-950°C) and time (1-8 h) on the phase purity of $BaTaO_2N$ were studied. As shown in Figures S3a and S3b, single-phase $BaTaO_2N$ with cubic perovskite structure (ICDD PDF 01-084-1748) was obtained at ≥900°C and ≥950°C by solid-state reaction and flux method, respectively, indicating the feasibility of solid-state reaction for the synthesis $BaTaO_2N$ at a lower temperature. In both cases, impurity phases, such as $Ba_5Ta_4O_{15}$ and Ta_2O_5,were simultaneously formed along with $BaTaO_2N$ up to ≤900°C and ≤950°C due to an insufficient supply of active nitriding species ($NH_{2(ads)}$, $NH_{(ads)}$, $N_{(ads)}$, etc.). Although the localized NH_3 delivery system minimized the dissociation of NH_3 into N_2 and H_2 before reaching and adsorbing on the synthesis mixture surface, it had less control of reaction efficiency of NH_3, which is strongly dependent on temperature and NH_3 flow rate.[25–27] The XRD results from time-dependent experiments conducted at 950°C reveal that single-phase $BaTaO_2N$ can be synthesized within ≥6 h and ≥4 h by solid-state reaction and flux method, respectively (Figures S4a and S4b), demonstrating the advantage of flux method in reducing the synthesis time. Such discrepancy in synthesis time is possibly stemmed from different repulsive adsorbate interactions affecting the diffusion rates of active nitriding species.[28] Previously, water-saturated NH_3[29] and a small amount of O_2[30] were successfully employed to control the equilibrium between the nitridation and reoxidation reactions during the synthesis of transition metal oxynitrides. Likewise, we have attempted to decrease the number of reduced tantalum species and defect density in $BaTaO_2N$ by employing water-saturated NH_3 (12.5 $L{\cdot}h^{-1}$ NH_3 + H_2O) and a small amount of O_2 (12.5 $L{\cdot}h^{-1}$ NH_3 + 1.2 $L{\cdot}h^{-1}$ O_2 and 12.5 $L{\cdot}h^{-1}$ NH_3 + 0.04 $L{\cdot}h^{-1}$ O_2) in solid-state reaction at 950°C for 10 h. As shown in Figure S5, none of these synthesis parameters led to the formation of $BaTaO_2N$ with a lower defect density. Instead, $Ba_5Ta_4O_{15}$ (ICDD PDF 01-072-0115, space group $P\bar{3}m1$ (no. 164), and lattice parameters: a = 5.7900 Å, b = 5.7900 Å and c = 11.7500 Å) was formed and remained the predominant phase and other minor phases, suggesting that even a small amount of oxygen and water molecules can interrupt the N-to-O exchange during the synthesis of $BaTaO_2N$.

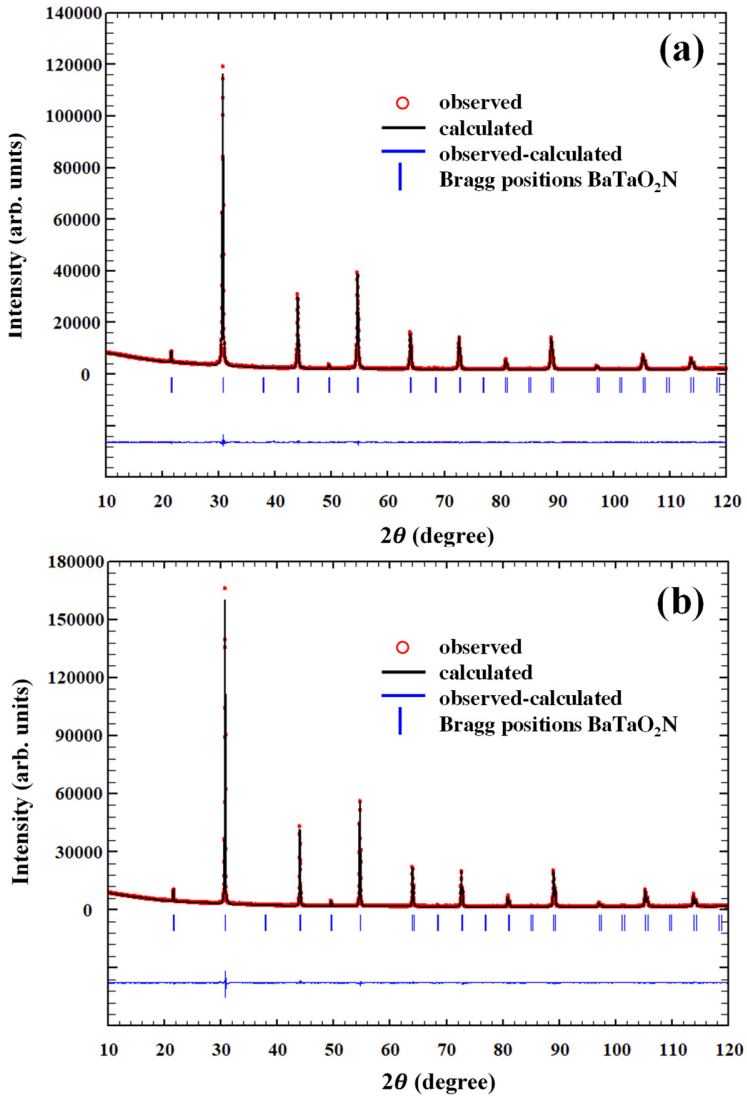

Figure 1. X-ray diffraction patterns of $BaTaO_2N$ samples synthesized by solid-state reaction (a) and flux method (b) with the results of the Rietveld refinement.

Rietveld refinements of the diffraction data (Figures 1a and 1b, Tables S1-S4) confirm the crystal structure of $BaTaO_2N$ in space group $Pm\bar{3}m$ for both samples synthesized by solid-state reaction and flux method at 950°C for 6 h followed by annealing at 700°C for 1 h in Ar. The site occupation factors were thereby kept fixed (for the cations and anions) to their ideal values determined by XPS and N/O hot gas extraction analyzer. Lattice parameters *a* of BTON-S(Ar) and BTON-F(Ar) are 4.11296(18) Å and 4.11158(13) Å, whereas unit cell volumes are 69.577(5) $Å^3$ and 69.506(4) $Å^3$, respectively. In agreement

with the previously reported lattice parameter of $BaTaO_2N$, because of the higher nitrogen content in the former, the lattice parameter *a* of BTON-S(Ar) is slightly higher than BTON-F(Ar), leading to the larger unit cell volume.[31] Thus, BTON-F(Ar) has much higher crystallinity and larger crystallite size due to favorable crystal growth free from mechanical and thermal strains in the completely ionized non-aqueous high-temperature solution (flux). As Kudo and Miseki stated,[32] high crystallinity is more advantageous than a high surface area for water oxidation and reduction reactions because the recombination of photogenerated charge carriers impedes uphill reactions. The higher crystallinity of BTON-F(Ar) is expressed inter alia by the splitting of individual reflections due to Cu-$K_{\alpha1}$ and Cu-$K_{\alpha2}$ radiation at lower diffraction angles compared to BTON-S(Ar).

To observe the influence of synthesis methods and annealing in Ar on morphology and size, the samples were examined by SEM. In Figure 2a, BTON-S particles with irregular shapes, unclear edges, and an average size of 128 nm were observed. In contrast, large plate-like hexagonal crystallites with well-developed facets, sharp edges, and an average size of 421 nm were seen along with idiomorphic crystallites with the size of 287 nm in BTON-F (Figure 2c). BTON-S consists of aggregated polycrystalline particles with massive grain boundaries stemmed from the solid-state reaction, which may function as recombination hubs for photogenerated charge carriers.[33,34] Conversely, BTON-F consists of highly crystalline and well-developed crystallites with fewer grain boundaries due to the flux method, facilitating the transfer and separation of charge carriers during photoelectrochemical water splitting.[35] Similarly, $BaTaO_2N$ synthesized using the RbCl flux suppressed charge recombination and facilitated the transfer of photogenerated electrons to the Pt cocatalyst for efficient H_2 evolution due to low density of structural defects and mid-gap states.[4] $BaTaO_2N$ crystallites exhibited more than two times higher O_2 evolution rate due to high crystallinity, reduced surface defect density, and fewer grain boundaries achieved by nitriding the $Ba_5Ta_4O_{15}$ crystallites in the KCl flux.[36] As shown in Figures 2b and 2d, the particle morphology remained unchanged, but the particle size was increased to 243 nm for BTON-S(Ar) and 432 nm for BTON-F(Ar) after annealing in Ar. The reduced surface defect density

achieved by annealing in Ar cannot be observed in the SEM images, and the samples were further subjected to TEM analysis.

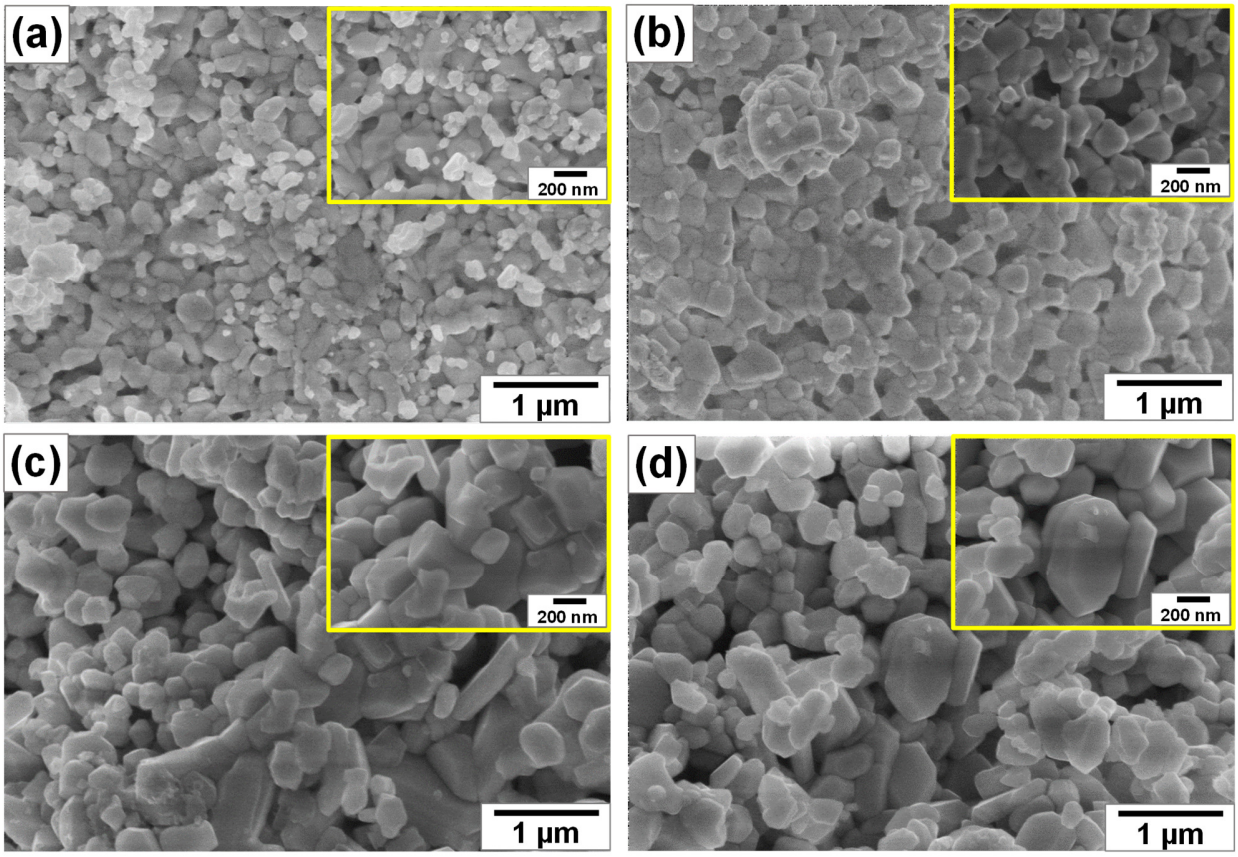

Figure 2. SEM images of $BaTaO_2N$ samples synthesized by solid-state reaction (a,b) and flux method (c,d) before and after thermal treatment in Ar.

To further investigate the influence of the synthesis methods on the crystalline nature and nanostructure, the $BaTaO_2N$ samples synthesized by solid-state reaction and flux method were characterized by transmission electron microscopy (TEM). Bright-field TEM, high-resolution TEM (HRTEM) images and selected area electron diffraction (SAED) patterns of the samples are shown in Figure 3. Smaller crystallites with unclear edges can be observed in the bright-field TEM images of BTON-S and BTON-S(Ar), whereas a large plate-like hexagonal crystallite with a sharp edge can be seen in the bright-field TEM images of BTON-F and BTON-F(Ar). In Figures 3a and 3b, the HRTEM images, taken near the

edge of the crystallites, show parallel lattice fringes with the spacing of 0.29 nm, which corresponds to the {110} interplanar distance of $BaTaO_2N$, with no clear defects in the observed range. The HRTEM images in Figures 3c and 3d also indicate that the spacing between the adjacent lattice fringes is 0.29 nm, which is consistent with the {110} interplanar distance of $BaTaO_2N$. Similarly, no clear bulk and surface defects were noted in the examined region of the crystallite, confirming the high crystallinity of the synthesized $BaTaO_2N$ samples. This also confirms the beneficial impact of annealing in Ar, which reduced the surface defects and improved the surface crystallinity.

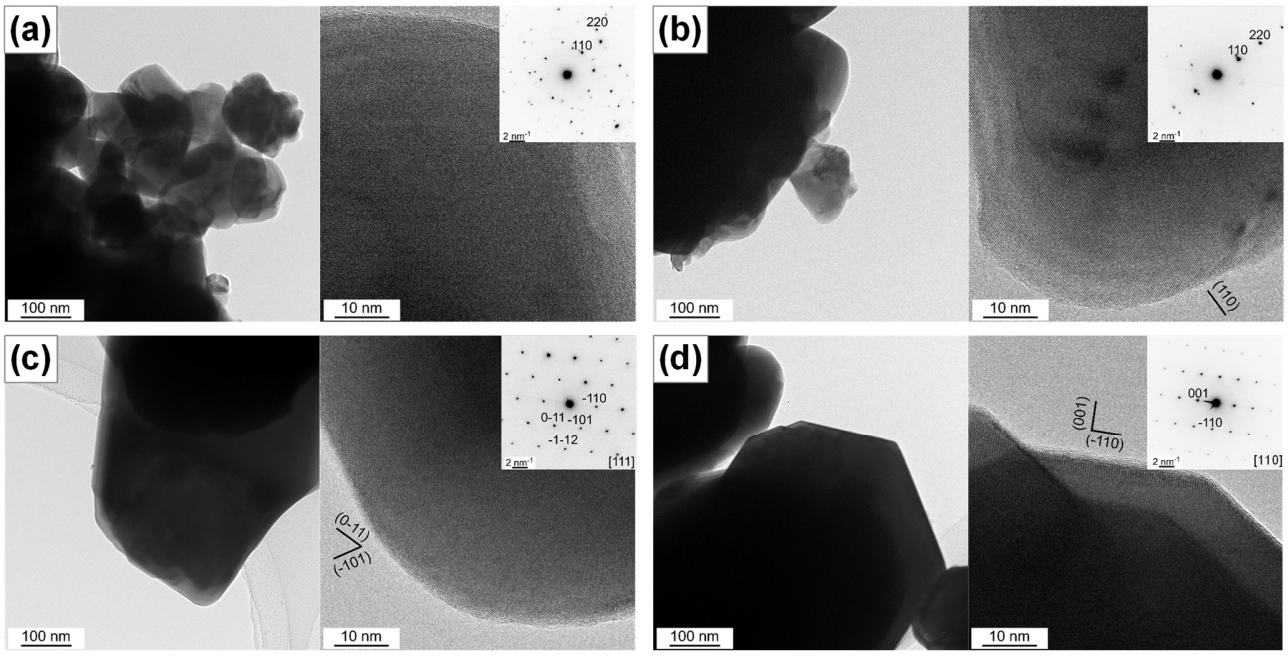

Figure 3. TEM and HRTEM images and SAED patterns of $BaTaO_2N$ samples synthesized by solid-state reaction (a,b) and flux method (c,d) before and after thermal treatment in Ar.

Random diffraction spots instead of regular diffraction spots can be observed in the SAED patterns in Figures 3a and 3b, representing the randomly oriented crystallites of BTON-S and BTON-S(Ar). In contrast, the highly ordered diffraction spots in the corresponding SAED patterns in Figure 3c and 3d, taken from the [111] and [110] directions of BTON, respectively, shows that the plate-like hexagonal crystallites of the BTON-F and BTON-F(Ar) have a well-developed single crystalline nature. The

observed diffraction spots can be indexed as $\overline{1}\overline{1}2$, $0\overline{1}1$, $\overline{1}10$, and $\overline{1}01$ for BTON-F, suggesting that the plate-like hexagonal crystallites have dominantly exposed {111} facets. The SEM and TEM results show that the morphology and size of $BaTaO_2N$ crystallites can be readily tailored by applying different synthesis methods. Therefore, the BTON-F and BTON-F(Ar) samples are expected to have a large lateral area for photon absorption, a greater number of active sites for water oxidation reaction, and a short travel distance to the surface for photogenerated charge carriers in comparison to the BTON-S and BTON-S(Ar) samples due to their plate-like morphology and single-crystalline nature.

The UV-Vis diffuse reflectance spectra of the $BaTaO_2N$ samples are shown in Figure 4, indicating a strong absorption in the visible range due to the electron transition from the valence band (N 2p and O 2p orbitals) to the conduction band (empty Ta 5d orbitals).[37] The onsets of light absorption of the as-synthesized BTON-F and BTON-S are located at <660 nm. Annealing in Ar led to a slight red shift in the absorption edges of BTON-F(Ar) and BTON-S(Ar) due to the reduction of the defect density and improved crystallinity, resulting in a slight optical band gaps reduction. The optical band gaps estimated using the Tauc plot method,[38] with an estimated standard deviation of $\pm$ 0.5 eV, are 2.01 eV for BTON-S, 1.95 eV for BTON-S(Ar), 2.05 eV for BTON-F, and 2.00 eV for BTON-F(Ar). The optical band gaps of $BaTaO_2N$ samples synthesized by solid-state reaction are slightly smaller than those of $BaTaO_2N$ samples synthesized by flux method. This is attributed to the higher nitrogen-to-oxygen ratio in BTON-S (N:O=0.44) and BTON-S(Ar) (N:O=0.46) in comparison to BTON-F (N:O=0.37) and BTON-F(Ar) (N:O=0.34), which were measured by a hot gas extraction analyzer. Additionally, the dark-brown powder color of BTON-S and BTON-S(Ar) also indicates the presence of higher nitrogen content and anionic deficiencies in comparison to the reddish-brown powder color of BTON-F and BTON-F(Ar). The higher nitrogen content led to a greater contribution of the N 2*p* levels to the upward shift of the valence band, narrowing the optical band gaps slightly. Recently, Widenmeyer et al.[39] proposed controlling an optical bandgap in perovskite-type $Eu_{1-x}Ca_xTiO_3$ from 2.56 eV to 2.22 eV via ammonolysis and partial Ca^{2+} substitution, where an important contribution of the nitrogen content on adjusting the optical band was

presented. Interestingly, no background absorption was observed in the UV-Vis diffuse reflectance spectra of the $BaTaO_2N$ samples synthesized in this study compared with previously reported $BaTaO_2N$,[40] suggesting a lower concentration of optically active defects.

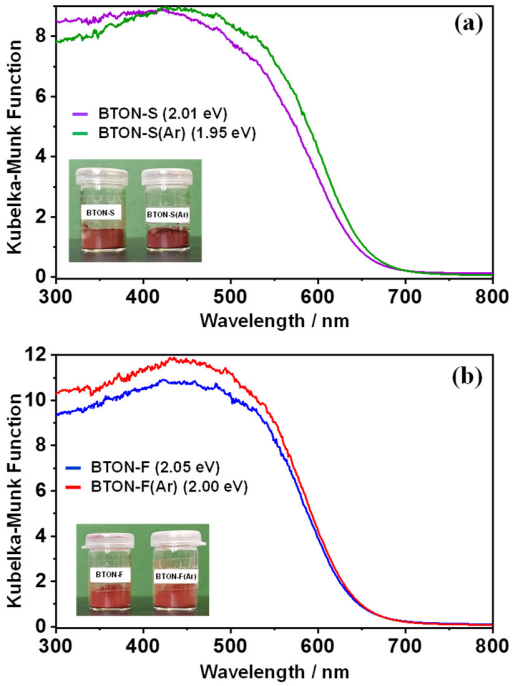

Figure 4. UV-Vis diffuse reflectance spectra of $BaTaO_2N$ samples synthesized by solid-state reaction (a) and flux method (b) before and after thermal treatment in Ar.

To further analyze the surface chemical states and compositions, the samples were characterized by X-ray photoelectron spectroscopy (XPS). The XPS core-level spectra of Ta 4f and O 1s of BTON-S, BTON-S(Ar), BTON-F, and BTON-F(Ar) are shown in Figure 5. The Ta 4f XPS core-level spectra reveal two doublets corresponding to the $4f_{7/2}$ and $4f_{5/2}$ spin-orbit split components upon deconvolution. The peaks observed at approximately 24.90-24.97 eV (Ta $4f_{7/2}$) and 26.78-27.02 eV (Ta $4f_{5/2}$) are attributed to the Ta–N bonds in the TaON and Ta_3N_5 structural units, whereas the peaks noted at approximately 25.79-26.05 eV (Ta $4f_{7/2}$) and 27.69-28.07 eV (Ta $4f_{5/2}$) are associated with the Ta–O bond in the TaON structural unit.[41,42] As shown in Table S5, the peak ratio of Ta–N:Ta–O was estimated to be 0.69, 1.22,

1.06, and 0.86 for BTON-S, BTON-S(Ar), BTON-F, and BTON-F(Ar), respectively, which is in good agreement with the N:O ratio analyzed by a hot gas extraction analyzer. Interestingly, high-temperature annealing in Ar partly released nitrogen from BTON-F in comparison to BTON-S.[16] The oxidation state of tantalum was confirmed to be +5, and no peaks assignable to reduced tantalum species could be found in the XPS spectra. The O 1s XPS core-level spectra of all samples can be mainly resolved into two Gaussian–Lorentzian components centered at 530.1-530.5 eV and 531.8-532.2 eV, which are assignable to the lattice oxygen (O_L) and oxygen vacancies or defects (O_V), respectively.[43] Interestingly, the O 1s XPS core-level spectrum of BTON-F has an additional component at 533.6 eV, indicating the higher number of chemisorbed or dissociated (O_C) oxygen species.[44] As shown, the intensity of the component at 533.6 eV was reduced after annealing in Ar, suggesting the reduced number of chemisorbed or dissociated (O_C) oxygen species. The XPS valence band spectra of all four samples in Figure S6 indicate the relative positions of the valence band maximum edges of BTON-S, BTON-S(Ar), BTON-F, and BTON-F(Ar) at 1.78, 1.77, 1.87, and 1.80 eV, respectively. A slightly negative shift in the valence band maximum was observed after annealing in Ar. This will be later used for comparing the band structures estimated from photoelectrochemical measurements.

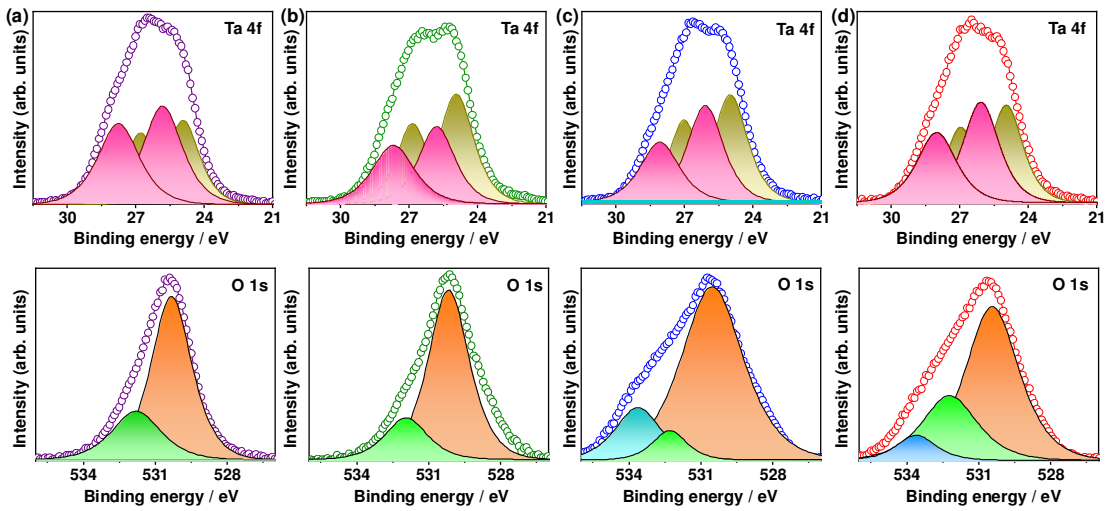

Figure 5. Narrow-scan Ta 4f (*top*) and O 1s (*bottom*) XPS spectra of $BaTaO_2N$ samples synthesized by solid-state reaction (a,b) and flux method (c,d) before (a,c) and after (b,d) Ar treatment.

The conversion of solar energy into chemical energy through the semiconductor-electrolyte interface is influenced by multiple factors.[45,46] The absorption of a photon by the electrode material is the first step that generates charge carriers: holes in the valence band (VB) and electrons in the conduction band (CB). The non-equilibrium condition changes the energy profile of the CB and VB, enabling the transfer of photogenerated charge carriers. For *n*-type semiconductors, photogenerated holes in the VB promote the oxygen evolution reaction, which is sustained by the extraction of photogenerated electrons in the CB to the external circuit to proceed with the hydrogen evolution reaction on the secondary electrode. The relationship between doping, structural change, and chemical composition often determines how light interacts with semiconductor materials, originating a complex dependence of the photoelectrochemical (PEC) response on optoelectronic properties.[47] To explore how the optoelectronic properties affect the electrochemical behavior, the photoanodes were fabricated using the BTON-F, BTON-F(Ar), BTON-S, and BTON-S(Ar) samples. In addition, the use of electrolytes at neutral pH suggests a safe and convenient application by requiring fewer reagents, such as acids and bases.[48,49] However, it is recognized that few materials carry out the water splitting under these conditions (neutral pH) because of losses resulted from overpotential concentration by pH gradients in large-scale operations.[49,50] It is essential to obtain information about materials that function at neutral pH and to understand their behavior for designing better applications. Therefore, the PEC studies were conducted in neutral pH electrolyte to understand charge transfer phenomena and charge carrier recombination in the synthesized $BaTaO_2N$ samples.[47,51]

Figure 6 shows the linear sweep voltammetries (LSV) and chronoamperometries (CA) of the BTON-F, BTON-F(Ar), BTON-S, and BTON-S(Ar) photoanodes under dark and light conditions. Generally, photocurrent is resolved under light irradiation due to the collection of photogenerated electrons, highlighting that the recorded current is kept at much lower values and close to zero in the dark. The current signal under light irradiation is sustained by the continuous oxidation of water on the surface of the photoanodes.[9,11] In Figure 6a, it can be seen that all the fabricated electrodes exhibit comparable

photocurrent values, and the highest photocurrent values were obtained for the BTON-F(Ar) in the full range of applied potentials. Such behavior is caused by a charge transfer favored with high overpotentials. Compared with the previously reported photocurrent densities of $BaTaO_2N$,[15,52] the photocurrent densities of the $BaTaO_2N$ samples in this study are lower due to different pH values of electrolyte solutions. It is important to mention that K_3PO_4 electrolyte (pH = 13) has been used in previous studies, while electrolyte based on Na_2SO_4 (pH around 7) was used in this study. Under the current conditions explored, various additives, such as hole scavengers, can be used to further increase the photocurrent values.[53] The characteristic shape of the photocurrent response as a function of potential indicates that the recombination phenomenon dominates at low overpotentials, while an exponential increase in the photocurrent is noted at high overpotentials. Such observation is consistent with the previous report, as it is known that the potential, where the photocurrent starts to increase over the BTON-F and BTON-S photoanodes, is more positive than the potential of the CB.[16] Figure 6b shows the photocurrent responses of the BTON-F and BTON-S photoanodes measured under repeated light-on and light-off conditions. Here, two aspects of relevance can be highlighted: (i) at high overpotentials, the photocurrent signal is resolved without delay when irradiating the surfaces, and when the flux of light stops, the photocurrent restores its value in the dark and (ii) the stationary photocurrent value under light irradiation follows the trend: BTON-F(Ar) > BTON-F > BTON-S(Ar) > BTON-S.

Figures 6c and 6d show the chronoamperometries in two different potentials: 1.23 V vs. RHE and 1.6 V vs. RHE, respectively. The photocurrents rapidly reach their stationary values, which are maintained as a function of time, suggesting the stability of the surfaces. Again, all the fabricated BTON-F and BTON-S photoanodes exhibit the photocurrent values in the same order of magnitude, and the BTON-F(Ar) electrode shows the highest photocurrent value. Here, the electrodes exhibiting a stationary behavior under the current light irradiation and an applied potential of 1.6 V vs RHE have a good stability under the operating conditions that can be considered extreme. To ensure such stability, Figure S7 shows the

current vs. time plot of the BTON-F(Ar) sample at different applied potentials (1.23 V vs. RHE and 1.6 V vs. RHE) under light irradiation for 900 min.

The detailed electrochemical study provides information on neutral pH electrolytic solutions, which allow to achieve stable photocurrent values for BTON-F(Ar) (0.35 μA·cm^{-2}) and BTON-F, BTON-S(Ar), and BTON-S (0.20 - 0.25 μA·cm^{-2}) electrodes at 1.23 V vs. RHE. For instance, the conversion efficiency of half-cell solar energy to hydrogen (HC-STH) (Eq. 2) was previously reported to reach 0.7% at 1.0 V vs. RHE for $BaTaO_2N$ photoanode materials.[9]

$$HC\text{-}STH = J \cdot (E_0 - E) / P_{light} \quad (2)$$

where J is the photocurrent density, E_0 is the reversible potential of water oxidation (1.23 V vs. RHE), E is the electrode potential, and P_{light} is the irradiance. To obtain information on the photoelectrochemical behavior (charge transfer versus recombination) of the BTON-F and BTON-S photoanodes, it is convenient to perform experiments at potentials around 1.23 V versus RHE and then the trends will be explored.

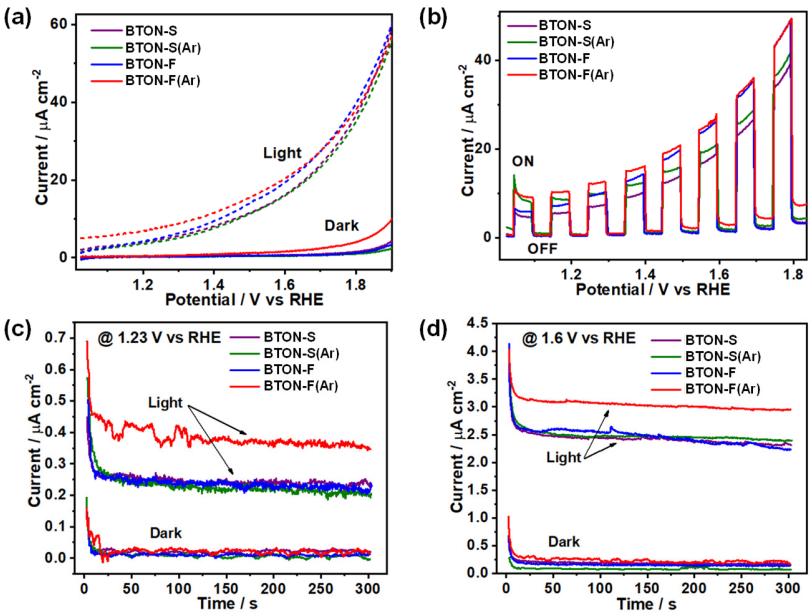

Figure 6. Linear sweep voltammetry (LSV) of $BaTaO_2N$ samples: (a) dark and light condition and (b) dark-light chopped condition. Cronoamperometry (CA) of $BaTaO_2N$ samples under dark and light conditions: (c) 1.23 V vs. RHE and (d) 1.6 V vs. RHE.

Although estimating the photocurrent values under visible light irradiation is important for new applications, understanding the nature of trends and other phenomena governing the photoelectrochemical behavior is essential to develop suitable design strategies for the successful implementation of photoanodes. Therefore, it is important to obtain more information on thermodynamics (e.g., the values of the energy potentials of the conduction and valence bands) and kinetics (e.g., the transfer and deactivation processes at the electrode-electrolyte interface).

In relation to the energy values, Figure S8 shows the Mott-Schottky (MS) plots of the BTON-F and BTON-S photoanodes. The linear variation of C^{-2} against the potential (E) indicates the accumulation of minority carriers in the space charge zone (SCZ) and adjusting by least squares to the MS equation:

$$C^{-2} = [2/(\varepsilon_0 \varepsilon e_0 N_D)] (E - E_F - k_B T/e_0) \quad (3)$$

where ε is the dielectric constant of the semiconductor, ε_0 is the vacuum permittivity, e_0 is the elementary charge, k_B is the Boltzmann constant, and T is the absolute temperature, and the values of charge carrier density (N_D) and flat band potential or Fermi level (E_F) were obtained.[45,51,54] For n-type semiconductors, the slope of the C^{-2} vs. E plot is positive and $E_F = E_{CB}$. Knowing that $E_g = E_{VB} - E_{CB,}$ it is possible to use the band gap value (E_g) measured experimentally by ultraviolet–visible spectroscopy to estimate the position of each energy band of the semiconductor electrode. Figure S9 shows the energy diagrams of BTON-F, BTON-F(Ar), BTON-S, and BTON-S(Ar), confirming that the E_{VB} values of the BTON-F and BTON-S photoanodes are more positive than the potential for water oxidation and the E_{CB} values of the BTON-F and BTON-S photoanodes are more negative than the potential for water reduction. Although the band gap values of the fabricated BTON-F and BTON-S photoanodes are similar, some differences are noted in the positions of the conduction and valence bands. These differences are due to the electronic characteristics defined from the applied synthesis methods of $BaTaO_2N$ samples. In fact, E_{VB}, E_{CB}, and the equilibrium potential change with the same trend. However, the equilibrium potential values in the dark reflect greater variations, which can also be interpreted as mid-gap states or surface states that are resolved from different synthesis methods. Briefly, the flux method resulted in more negative equilibrium

potential (0.85 V for BTON-S(Ar) vs. 0.82 V for BTON-F(Ar) and 0.78 V for BTON-S vs. 0.77 V for BTON-F), while annealing in Ar led to the shift of the equilibrium potential towards more positive values (0.78 V for BTON-F vs. 0.82 V for BTON-F(Ar) and 0.77 V for BTON-S vs. 0.85 V for BTON-S(Ar)). This is evident in the first zone of the open circuit potential curves, which will be discussed later. Then, there must also be differences in the kinetic behavior to elucidate the effect of the changes in $BaTaO_2N$ samples seemed from different synthesis methods.

Figure 7 shows the chronoamperometry profiles measured under chopped light irradiation at different electrode potentials: equilibrium potential (around 0.8 V vs. RHE) (a), 1.23 V vs. RHE (b), and 1.6 V vs. RHE (c). From the shape of the transient photocurrent responses, three significant aspects are revealed: (i) the typical results of increasing the magnitude of the full transient photocurrent by increasing the potential (comparison between Figures 7a, 7b, and 7c), (ii) at the equilibrium potential the trend in the magnitude of the transient photocurrent of the BTON-F electrodes (Figure 7a) is well defined, highlighting that for higher potentials the relative difference between the electrodes decreases (Figures 7b and 7c), and (iii) at the equilibrium potential the transient photocurrents of the BTON-F photoanodes exhibit spikes followed by decay after light irradiation and a negative overshoot after imposing the dark condition effect (Figure 7a), which is minimized at higher potentials. From the above aspects, we further focus on the third aspect.

Generally, spikes and overshoots observed in the transient photocurrent response to chopped light irradiation are interpreted as evidence for the surface recombination.[44,55] However, during the water-splitting reaction, it is possible that the kinetics of the electron transfer reactions are sluggish that the concentration of minority carriers around the surface increases to very high values. This phenomenon modifies the potential drop across the Helmholtz layer in the electrolyte, leading to “unpinning the edge of the band”.[55] Both phenomena, the recombination on the surface or slow kinetics for the water-splitting reaction, impose severe kinetic limitations on the conversion of solar energy into photo-redox reactions

in addition to the crystallinity, defect density, grain boundaries, and surface properties of the fabricated photoanodes.

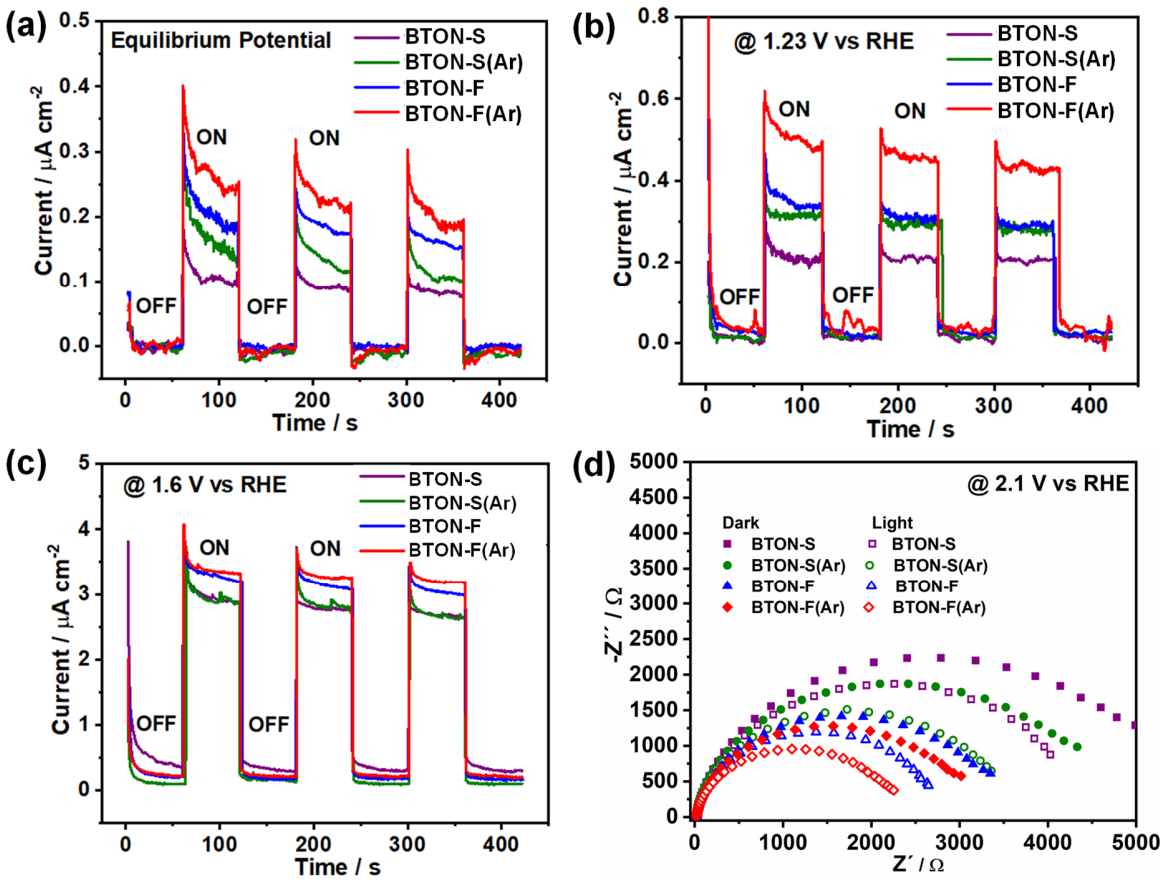

Figure 7. Cronoamperometry profiles of $BaTaO_2N$ samples under chopped condition: (a) equilibrium potential (0.8 V vs. RHE), (b) 1.23 V vs. RHE and (c) 1.6 V vs. RHE. (d) Electrochemical impedance spectroscopy (EIS) of $BaTaO_2N$ samples: Nyquist plot 2.1 V vs. RHE.

Figure 7d shows the Nyquist plots of the BTON-F and BTON-S photoanodes in both dark and light conditions. For the same photoanode, a semicircle signal with a smaller radius is observed under light irradiation compared to the semicircle signal with a larger radius observed in the dark. By comparing the semicircle signals of the fabricated photoanodes under light irradiation, it can be noted that the charge transfer resistance at the interface between the electrolyte and the BTON-F electrodes decreases. This is consistent with a relative increase in the efficiency of electron transfer of the fabricated photoanodes:

BTON-F(Ar) > BTON-F > BTON-S(Ar) > BTON-S, which corresponds to the trend observed in the LSV and CA measurements. In fact, the effects observed on the photocurrent during the oxidation of water can be associated with the crystallinity, defect density, grain boundaries, and surface properties[56,57] of the BTON-F and BTON-S samples achieved through the proposed synthesis approach.

From the analysis of the transient potentials in the open circuit condition and perturbed by dark-light-dark conditions, it is possible to obtain more information about the dynamic effects that deactivate the charge carriers in addition to revealing the trends related to the crystallinity, defect density, grain boundaries, and surface properties of the BTON-F and BTON-S photoanodes.[47] Figure 8a shows the open circuit potential (E_{OC}) vs. time under dark-light-dark conditions for all photoanodes. The E_{OC} values indicate the steady-state concentration of photogenerated charge carriers, and their transient reflects interesting variations.[47,58] First, the E_{OC} starts from a stationary potential for all photoanodes, and the main difference in the initial E_{OC} values is related to the variation in crystallinity, defect density, grain boundaries, and surface properties of the fabricated photoanodes. Then, under light irradiation, the decrease in potential defines a transient reflecting the difference between the energy profiles of the photoanodes. Thus, corroborating the kinetic limitations discussed above from the analysis of photocurrent transients or chronoamperometry. Finally, when the light was turned off in all systems, the potential relaxes with relatively slow kinetics, implying that the deactivation occurs because of phenomena that influence the energetics of the conduction and valence bands. The lifetime (τ) of charge carriers can be evaluated from the last stage of the E_{OC} vs. time profiles by using the following equation:[58]

$$\tau = |k_B T/e_0 \, (dE_{OC}/dt)^{-1}| \quad (4)$$

Figure 8b shows the lifetime vs. open circuit potential decay plots of the photoanodes. The observed trends between the electrodes are quite clear, indicating longer lifetimes in many potential values for the BTON-F(Ar) photoanode. Furthermore, for all the photoanodes, it is observed that the semi-logarithmic plot of lifetimes vs. E_{OC} (Figure 8b) reflects at least two phenomena that are manifested in changes of

slopes. The first zone has a high slope and occurs at low potential values, while the second zone encompasses the higher potentials and is clearly linear. The meeting potentials of these two trends are 0.602 V for BTON-F(Ar), 0.646 V for BTON-F, 0.625 V for BTON-S(Ar), and 0.669 V for BTON-S. In any case, under the studied conditions, the linear variation of the lifetime with the potential (in semi-logarithmic coordinates) turns out to be the one found in the highest proportion. The latter is consistent with the effect of the electrode potential on the (photo)electrochemical kinetics.[58] In any case, it is shown that different synthesis methods of $BaTaO_2N$ samples led to the changes in their density of states, which, in turn, mainly affected the kinetic properties of photoredox processes, including the recombination processes on the surfaces of photoanodes. This clearly shows that optoelectronic and surface properties, which dominate the carrier deactivation phenomena, can be modified by changing the synthesis method and synthesis parameters of $BaTaO_2N$. The effect of the electrode potential is key, which allowed solving trends and showing the inverse relationship between recombination and charge-transfer phenomena.

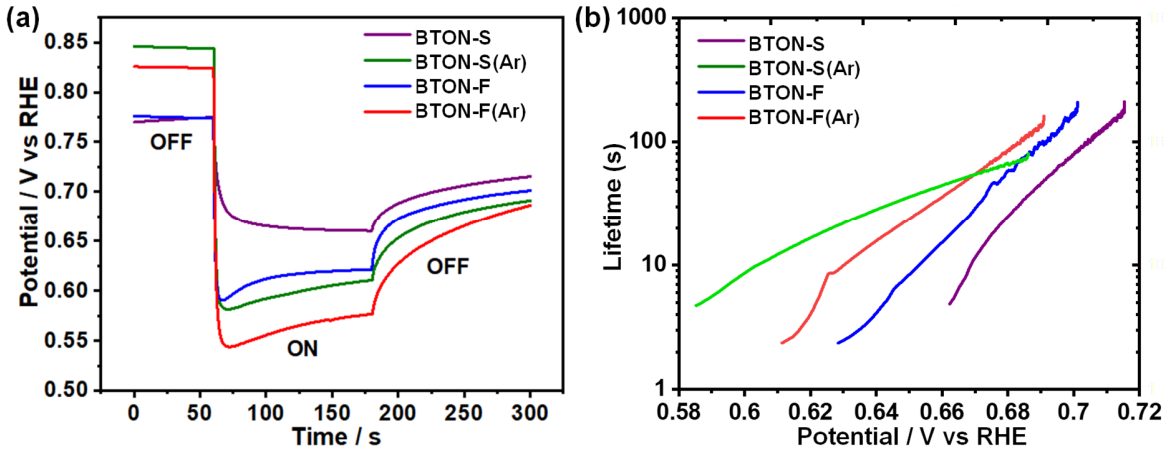

Figure 8. (a) Open circuit potential vs. time under dark–light–dark condition and (b) lifetime vs. open circuit potential decay plot of $BaTaO_2N$ samples synthesized by solid-state reaction and flux method before and after thermal treatment in Ar.

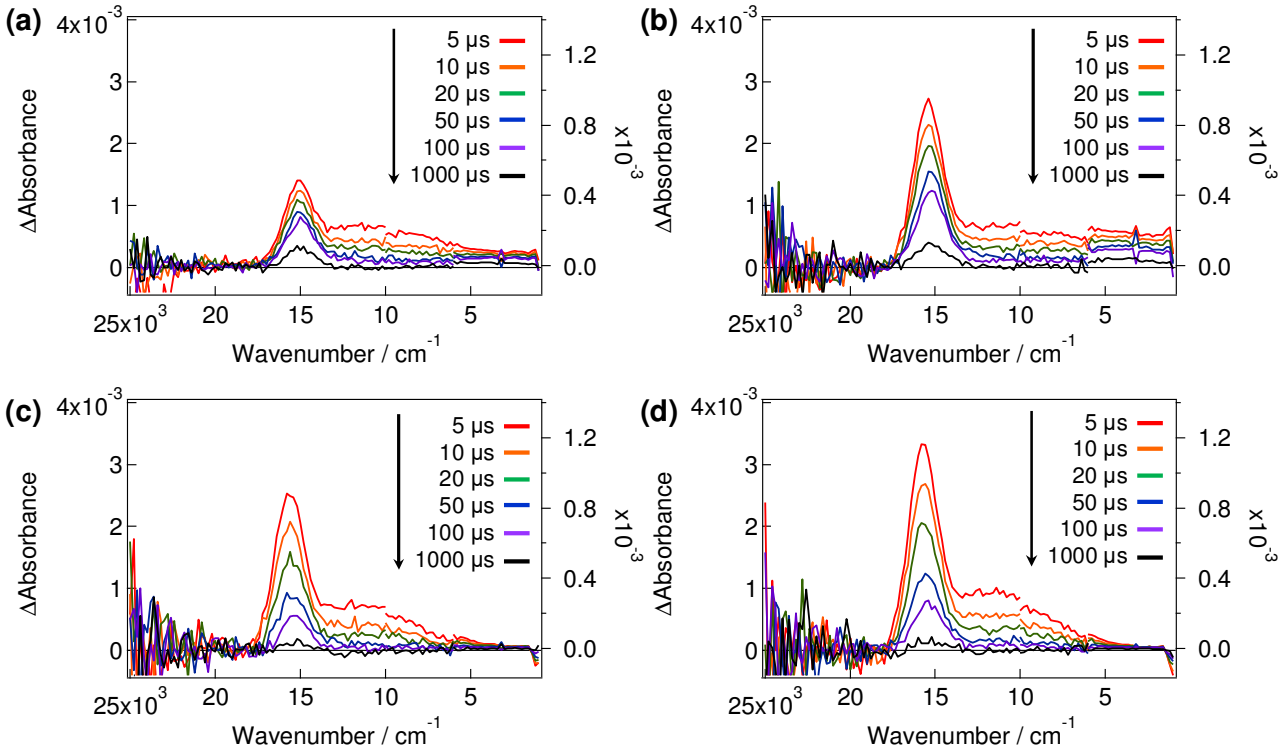

Figure 9. Transient absorption spectra of $BaTaO_2N$ samples synthesized by solid-state reaction (a,b) and flux method (c,d) before and after thermal treatment in Ar, irradiated by UV laser pulses (355 nm, 6 ns, 0.5 mJ per pulse, and 5 Hz, measured in vacuum).

Further, to gain insights into the impact of synthesis methods (solid-state reaction and flux method) in localized NH_3 delivery system on the complex nature and dynamics of photogenerated charge carriers, including free electrons, trapped electrons, and holes, the $BaTaO_2N$ samples were comparatively investigated by transient absorption spectroscopy (TAS)[4,59-61] on the femtosecond to second-time scale to correlate with their photoelectrochemical water oxidation activities. The TA spectra of BTON-S, BTON-S(Ar), BTON-F, and BTON-F(Ar), measured under irradiation by UV laser pulses (355 nm, 6 ns, 0.5 mJ per pulse, and 5 Hz, in vacuum), are shown in Figure 9. The TA spectra of all samples have three similar spectral regions: (i) the intensive absorption peaks at 17000-14000 cm^{-1} are associated with photogenerated holes, (ii) the broad absorption peaks at 14000-4000 cm^{-1} are assigned to the deeply trapped electrons and/or holes at the defects, and (iii) the broad absorption peaks at below 4000 cm^{-1} are

ascribed to the shallowly trapped electrons and/or free electrons. Obviously, the intensity of the absorption peaks in the first region (17000-14000 cm^{-1}), which are assigned to holes,[4] is increased after annealing in Ar and varied in the following order: BTON-F(Ar) > BTON-F > BTON-S(Ar) > BTON-S. This suggests that the flux method and annealing in Ar enabled BTON-F(Ar) to have the highest number of photogenerated holes despite having a similar number of deeply trapped charge carriers in the near-IR region. This is in good agreement with the PEC performance of the $BaTaO_2N$ samples.

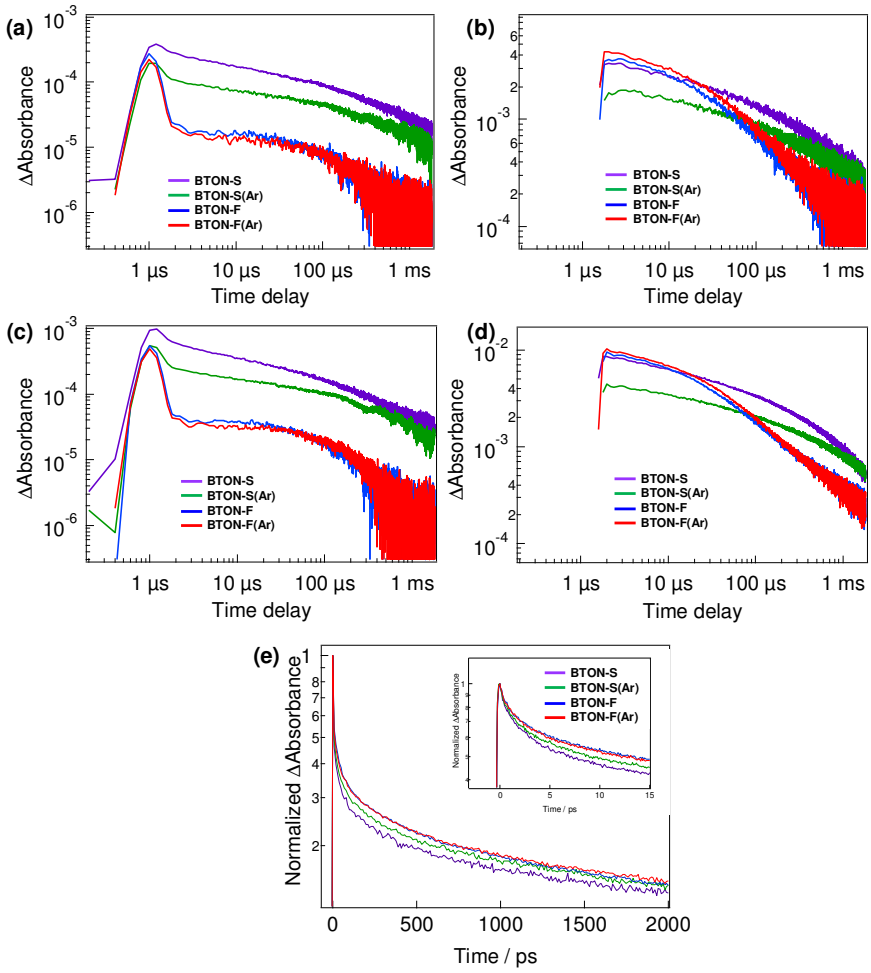

Figure 10. Decay curves of transient absorption of $BaTaO_2N$ samples, irradiated by UV laser pulses (355 nm, 6 ns, 0.5 mJ per pulse, and 5 Hz, measured in vacuum) and probed at 2000 cm^{-1} (a) and 15400 cm^{-1} (b) in a vacuum; irradiated by Vis laser pulses (480 nm, 6 ns, 5 mJ per pulse, and 5 Hz, measured in vacuum) and probed at 2000 cm^{-1} (c) and 15400 cm^{-1} (d) in a vacuum; and irradiated by UV laser pulses (355 nm, 90 fs, 6 μJ per pulse, and 500 Hz, measured in air) and probed at 15400 cm^{-1} (e).

For the further detailed analysis of decay kinetics of photogenerated electrons and holes in the $BaTaO_2N$ samples, the change in the intensity of a monochromatic probe light at 2000 cm^{-1} and 15400 cm^{-1} were monitored as a function of time after pump pulse irradiation. In Figure 10a-d, the TA results, measured under irradiation by UV and Vis laser pulses (355 nm and 480 nm, 6 ns, 0.5 and 5 mJ per pulse, and 5 Hz, measured in vacuum), reveal that the initial intensity of transient absorption probed at 15400 cm^{-1} is larger for BTON-F and BTON-F(Ar) compared with BTON-S and BTON-S(Ar), but more rapidly decays after 10 μs. The similar two-step rapid decay in μs is also observed for the transient absorption probed at 2000 cm^{-1}. These results indicate that the high mobility of charge carriers in BTON-F and BTON-F(Ar) samples accerelates the recombination after a few μs. As Kato and Yamakata[62] reported, the high mobility of charge carriers could prevent the initial fast recombination but accelerate the recombination in a slower time region since high crystallinity has dual effects (acceleration and deceleration) depending on the time region. Therefore, the acceleration in the slower time region may not be good for photocatalytic water splitting, but the prevention of the initial fast recombination would be beneficial for photoelectrochemical water splitting since charge carriers can readily move out to the outer electrodes or on the surface through the depletion layer when potential is applied. Interestingly, the TA results, measured under irradiation by UV laser pulses (355 nm, 90 fs, 6 μJ per pulse, and 500 Hz, measured in air) in Figure 10e show that the decay of the transient absorption probed at 15400 cm^{-1} is slower for BTON-F and BTON-F(Ar) compared with BTON-S and BTON-S(Ar), suggesting that the recombination of charge carriers in fs~ps region is also prevented in the BTON-F and BTON-F(Ar) samples due to their high crystallinity achieved by applying the flux synthesis method. The TAS results corroborating the higher number of surviving holes and efficient transfer of photogenerated charge carriers in the BTON-F and BTON-F(Ar) compared with BTON-S and BTON-S(Ar) are in good agreement with the PEC performance of the synthesized $BaTaO_2N$ samples. Finally, understanding the aforementioned kinetic limitations in stable photoanodes that function under visible light irradiation and using inexpensive electrolytes (such as water at neutral pH) allows to advance in finding suitable

functional materials and photoredox reaction conditions for efficient and stable green hydrogen generation from photoelectrochemical water splitting.

4. CONCLUSIONS

We have successfully reduced the synthesis time and defect density of $BaTaO_2N$ by localizing an NH_3 delivery system just above the synthesis mixture. Using such localized NH_3 delivery system, the generation of N_2 and H_2 was significantly minimized, and more active nitriding species were supplied. As a result, single-phase $BaTaO_2N$ with high crystallinity and low defect density was synthesized at 950°C for ≥6 h and ≥4 h by solid-state reaction and flux method, respectively, indicating the advantage of flux method over solid-state reaction in this system. It was found that $BaTaO_2N$ synthesized by flux method exhibited higher electron transfer characteristics than its counterpart synthesized by solid-state reaction. Carrier deactivation phenomena limit the response and can be modified by changing the synthesis method and synthesis parameters of $BaTaO_2N$. The demonstrated method can potentially be applied to the time-retrenched synthesis of other transition metal (oxy)nitrides with high crystallinity and low defect density to enhance their solar water splitting performance.

ASSOCIATED CONTENT:

Supporting Information

The Supporting Information is available free of charge at thttps://pubs.acs.org. Details of characterization methods and photoelectrochemical measurements. Results of the Rietveld refinement and refined atomic parameters for $BaTaO_2N$ synthesized via solid state synthesis and flux method (standard deviations in parenthesis). Binding energies of Ta 4f5/2 and Ta 4f7/2 peaks and peak areas of the synthesized samples. Schematic representations of a generally used NH_3 flow system for the synthesis of transition metal (oxy)nitrides and a localized NH_3 delivery system in this study. Synthesis procedures of $BaTaO_2N$ by solid-state reaction and flux method. X-ray diffraction patterns of $BaTaO_2N$ samples synthesized by solid-state reaction and flux method at different temperatures for 8 h and at 950°C for different times. X-

ray diffraction patterns of the samples synthesized by solid-state reaction at 950°C for 10 h under 12.5 $L \cdot h^{-1}$ NH_3 + 1.2 $L \cdot h^{-1}$ O_2, 12.5 $L \cdot h^{-1}$ NH_3 + 0.04 $L \cdot h^{-1}$ O_2, and 12.5 $L \cdot h^{-1}$ NH_3 + H_2O. XPS valence band spectra. Chronoamperometries (CA) of the BTON-F(Ar) sample at 1.23 V vs. RHE and 1.6 V vs. RHE under light irradiation for 900 min. Mott-Schottky plots and energy band positions of BTON-F, BTON-F(Ar), BTON-S, and BTON-S(Ar).

ACKNOWLEDGMENTS:

Authors would like to thank Dr. Stefan Berendts (TU Berlin) for O/N analysis, M.Sc. Ina Remy-Speckmann (TU Berlin) for X-ray diffraction analysis, Dipl. Phys. Christoph Fahrenson (ZELMI, TU Berlin) for SEM analysis, and Ms. Reiko Shiozawa (Shinshu University) for XPS analysis. This project has received funding from the European Union's Horizon 2020 research and innovation programme under the Marie Sklodowska-Curie grant agreement no. 793882.

REFERENCES:

(1) Grätzel, M. Photoelectrochemical cells. *Nature* **2001**, *414*, 338–344.
(2) Lewis, N. S.; Nocera, D. G. Powering the planet: Chemical challenges in solar energy utilization. *Proc. Natl Acad. Sci. USA* **2006**, *103*, 15729–15735.
(3) Walter, M. G.; Warren, E. L.; McKone, J. R.; Boettcher, S. W.; Mi, Q.; Santori, E. A.; Lewis, N. S. Solar Water Splitting Cells. *Chem. Rev.* **2010**, *110*, 6446–6473.
(4) Wang, Z.; Luo, Y.; Hisatomi, T.; Vequizo, J. J. M.; Suzuki, S.; Chen, S.; Nakabayashi, M.; Lin, L.; Pan, Z.; Kariya, N.; Yamakata, A.; Shibata, N.; Takata, T.; Teshima, K.; Domen, K. Sequential cocatalyst decoration on $BaTaO_2N$ towards highly-active Z-scheme water splitting. *Nature Commun.* **2021**, *12*, 1005.
(5) Abdi, F. F.; Han, L.; Smets, A. H. M.; Zeman, M.; Dam, B.; van de Krol, R. Efficient solar water splitting by enhanced charge separation in a bismuth vanadate-silicon tandem photoelectrode. *Nature Commun.* **2013**, *4*, 2195.
(6) van de Krol, R. Principles of Photoelectrochemical Cells, In Photoelectrochemical Hydrogen Production, Eds. R. van de Krol and M. Grätzel, Springer, 2012, pp. 13–68.
(7) Song, J.; Wei, C.; Huang, Z.-F.; Liu, C.; Zeng, L.; Wang, X.; Xu, Z. J. A review on fundamentals for designing oxygen evolution electrocatalysts. *Chem. Soc. Rev.* **2020**, *49*, 2196–2214.
(8) Jadhav, S.; Hasegawa, S.; Hisatomi, T.; Wang, Z.; Seo, J.; Higashi, T.; Katayama, M.; Minegishi, T.; Takata, T.; Peralta-Hernandez, J. M.; Torres, O. S.; Domen, K. Efficient photocatalytic oxygen evolution using $BaTaO_2N$ obtained from nitridation of perovskite-type oxide. *J. Mater. Chem. A* **2020**, *8*, 1127–1130.
(9) Ueda, K.; Minegishi, T.; Clune, J.; Nakabayashi, M.; Hisatomi, T.; Nishiyama, H.; Katayama, M.; Shibata, N.; Kubota, J.; Yamada, T.; Domen, K. Photoelectrochemical Oxidation of Water Using $BaTaO_2N$ Photoanodes Prepared by Particle Transfer Method. *J. Am. Chem. Soc.* **2015**, *137*, 2227–2230.

(10) Kim, Y.-I.; Woodward, P. M.; Baba-Kishi, K. Z.; Tai, C. W. Characterization of the Structural, Optical, and Dielectric Properties of Oxynitride Perovskites AMO_2N (A = Ba, Sr, Ca; M = Ta, Nb). *Chem. Mater.* **2004**, *16*, 1267–1276.
(11) Wang, C.; Hisatomi, T.; Minegishi, T.; Wang, Q.; Zhong, M.; Katayama, M.; Kubota, J.; Domen, K. Synthesis of Nanostructured $BaTaO_2N$ Thin Films as Photoanodes for Solar Water Splitting. *J. Phys. Chem. C* **2016**, *120*, 15758–15764.
(12) Maeda, K.; Domen, K. Water Oxidation Using a Particulate $BaZrO_3$-$BaTaO_2N$ Solid-Solution Photocatalyst That Operates under a Wide Range of Visible Light. *Angew. Chem. Int. Ed.* **2012**, *51*, 9865–9869.
(13) Higashi, M.; Domen, K.; Abe, R. Fabrication of an Efficient $BaTaO_2N$ Photoanode Harvesting a Wide Range of Visible Light for Water Splitting. *J. Am. Chem. Soc.* **2013**, *135*, 10238–10241.
(14) Pihosh, Y.; Nandal, V.; Minegishi, T.; Katayama, M.; Yamada, T.; Seki, K.; Sugiyama, M.; Domen, K. Development of a Core-Shell Heterojunction Ta_3N_5-Nanorods/$BaTaO_2N$ Photoanode for Solar Water Splitting. *ACS Energy Lett.* **2020**, *5*, 2492–2497.
(15) Nishimae, S.; Mishima, Y.; Nishiyama, H.; Sasaki, Y.; Nakabayashi, M.; Inoue, Y.; Katayama, M.; Domen, K. Fabrication of $BaTaO_2N$ Thin Films by Interfacial Reactions of $BaCO_3$/Ta_3N_5 Layers on a Ta Substrate and Resulting High Photoanode Efficiencies During Water Splitting. *Sol. RRL* **2020**, **4**, 1900542.
(16) Seo, J.; Nakabayashi, M.; Hisatomi, T.; Shibata, N.; Minegishi, T.; Domen, K. Solar-Driven Water Splitting over a $BaTaO_2N$ Photoanode Enhanced by Annealing in Argon. *ACS Appl. Energy Mater.* **2019**, *2*, 5777–5784.
(17) Lan, Z.; Vegge, T.; Castelli, I.E. Theoretical Insight on Anion Ordering, Strain, and Doping Engineering of the Oxygen Evolution Reaction in $BaTaO_2N$. *Chem. Mater.* **2021**, *33*, 3297–3303.
(18) Pihosh, Y.; Minegishi, T.; Nandal, V.; Higashi, T.; Katayama, M.; Yamada, T.; Sasaki, Y.; Seki, K.; Suzuki, Y.; Nakabayashi, M.; Sugiyama, M.; K. Domen. Ta_3N_5-Nanorods enabling highly efficient water oxidation via advantageous light harvesting and charge collection. *Energy Environ. Sci.* **2020**, *13*, 1519–1530.
(19) Higashi, T.; Sasaki, Y.; Kawase, Y.; Nishiyama, H.; Katayama, M.; Takanabe, K.; Domen, K. Surface-Modified Ta_3N_5 Photoanodes for Sunlight-Driven Overall Water Splitting by Photoelectrochemical Cells. *Catalysts* **2021**, *11*, 584.
(20) Higashi, T.; Nishiyama, H.; Suzuki, Y.; Sasaki, Y.; Hisatomi, T.; Katayama, M.; Minegishi, T.; Seki, K.; Yamada, T.; Domen, K. Transparent Ta_3N_5 Photoanodes for Efficient Oxygen Evolution toward the Development of Tandem Cells. *Angew. Chem.* **2019**, *131*, 2322–2326.
(21) Page, K.; Stoltzfus, M. W.; Kim, Y.-I.; Proffen, T.; Woodward, P. M.; Cheetham, A. K.; Seshadri, R. Local Atomic Ordering in $BaTaO_2N$ Studied by Neutron Pair Distribution Function Analysis and Density Functional Theory. *Chem. Mater.* **2007**, *19*, 4037–4042.
(22) Hosono, A.; Masubuchi, Y.; Yasui, S.; Takesada, M.; Endo, T.; Higuchi, M.; Itoh, M.; Kikkawa, S. Ferroelectric $BaTaO_2N$ Crystals Grown in a $BaCN_2$ Flux. *Inorg. Chem.* **2019**, *58*, 16752−16760.
(23) Hojamberdiev, M.; Yubuta, K.; Vequizo, J. J. M.; Yamakata, A.; Oishi, S.; Domen, K.; Teshima, K. NH_3-Assisted Flux Growth of Cube-like $BaTaO_2N$ Submicron Crystals in a Completely Ionized Nonaqueous High-Temperature Solution and Their Water Splitting Activity. *Cryst. Growth Des.* **2015**, *15*, 4663–4671.
(24) Hojamberdiev, M.; Zahedi, E.; Nurlaela, E.; Kawashima, K.; Yubuta, K.; Nakayama, M.; Wagata, H.; Minegishi, T.; Domen, K.; Teshima, K. The cross-substitution effect of tantalum on the visible-light-driven water oxidation activity of $BaNbO_2N$ crystals grown directly by an NH_3-assisted flux method. *J. Mater. Chem. A* **2016**, *4*, 12807–12817.
(25) Rahinov, I.; Ditzian, N.; Goldman, A.; Cheskis, S. NH_2 Radical Formation by Ammonia Pyrolysis in a Temperature Range of 800–1000 K. *Appl. Phys. B* **2003**, *77*, 541–546.

(26) Odochian, L.; Dirtu, D.; Mocanu, A. M.; Moldoveanu, C. Contributions to the Degenerated Branching Mechanism of the Thermal Decomposition of Ammonia. *Kinetics Catal.* **2011**, *52*, 480–486.
(27) Mesrine, M.; Grandjean, N.; Massies, J. Efficiency of NH_3 as nitrogen source for GaN molecular beam epitaxy. *Appl. Phys. Lett.* **1998**, *72*, 350.
(28) Adamsen, K. C.; Kolsbjerg, E. L.; Koust, S.; Lammich, L.; Hammer, B.; Wendt, S.; Lauritsen, J. V. NH_3 on anatase TiO_2(101): Diffusion mechanisms and the effect of intermolecular repulsion. *Phys. Rev. Mater.* **2020**, *4*, 121601(R).
(29) Schilling, H.; Lerch, M.; Börger, A.; Becker, K.-D.; Wolff, H.; Dronskowski, R.; Bredow, T.; Tovar, M.; Baehtz, C. A new anatase-type phase in the system Mg–Ta–O–N. *J. Solid State Chem.* **2006**, *179*, 2416–2425.
(30) Lüdtke, T.; Schmidt, A.; Göbel, C.; Fischer, A.; Becker, N.; Reimann, C.; Bredow, T.; Dronskowski, R.; Lerch, M. Synthesis and Crystal Structure of δ-TaON, a Metastable Polymorph of Tantalum Oxide Nitride. *Inorg. Chem.* **2014**, *53*, 11691−11698.
(31) Pors, F.; Marchand, R.; Laurent, Y.; Bacher, P.; Roult, G. Etude structurale des perovskites oxyazotees $BaTaO_2N$ et $BaNbO_2N$: Structural study of $BaTaO_2N$ and $BaNbO_2N$ oxynitrided perovskites. *Mater. Res. Bull.* **1988**, *23*, 1447−1450.
(32) Kudo, A.; Miseki, Y. Heterogeneous photocatalyst materials for water splitting. *Chem. Soc. Rev.* **2009**, *38*, 253–278.
(33) Wang, Z.; Inoue, Y.; Hisatomi, T.; Ishikawa, R.; Wang, Q.; Takata, T.; Chen, S.; Shibata, N.; Ikuhara, Y.; Domen, K. Overall water splitting by Ta_3N_5 nanorod single crystals grown on the edges of $KTaO_3$ particles. *Nature Catal.* **2018**, *1*, 756–763.
(34) Wang, C. W.; Yang, S.; Fang, W. Q.; Liu, P.; Zhao, H.; Yang, H. G. Engineered Hematite Mesoporous Single Crystals Drive Drastic Enhancement in Solar Water Splitting. *Nano Lett.* **2016**, *16*, 427–433.
(35) Wang, S.; Liu, G.; Wang, L. Crystal Facet Engineering of Photoelectrodes for Photoelectrochemical Water Splitting. *Chem. Rev.* **2019**, *119*, 5192–5247.
(36) Hojamberdiev, M.; Kawashima, K.; Hisatomi, T.; Katayama, M.; Hasegawa, M.; Domen, K.; Teshima, K. Distinguishing the effects of altered morphology and size on the visible light induced water oxidation activity and photoelectrochemical performance of $BaTaO_2N$ crystal structures. *Faraday Discuss.* **2019**, *215*, 227–241.
(37) Maeda, K.; Lu, D.; Domen, K. Oxidation of Water under Visible-Light Irradiation over Modified $BaTaO_2N$ Photocatalysts Promoted by Tungsten Species. *Angew. Chem. Int. Ed.* **2013**, *52*, 6488–6491.
(38) Tauc, J.; Grigorovici, R.; Vancu, A. Optical Properties and Electronic Structure of Amorphous Germanium. *Phys. Status Solidi B* **1966**, *15*, 627–637.
(39) Widenmeyer, M.; Kohler, T.; Samolis, M.; De Denko, A. T.; Xiao, X.; Xie, W.; Osterloh, F. E.; Weidenkaff, A. Band Gap Adjustment in Perovskite-type$Eu_{1-x}Ca_xTiO_3$ via Ammonolysis. *Z. Phys. Chem.* **2020**, *234*, 887–909.
(40) Dong, B.; Qi, Y.; Cui, J.; Liu, B.; Xiong, F.; Jiang, X.; Li, Z.; Xiao, Y.; Zhang, F.; Li, C. Synthesis of $BaTaO_2N$ oxynitride from Ba-rich oxide precursor for construction of visible-light-driven Z-scheme overall water splitting. *Dalton Trans.* **2017**, *46*, 10707–10713.
(41) Ma, Z.; Jaworski, A.; George, J.; Rokicinska, A.; Thersleff, T.; Budnyak, T. M.; Hautier, G.; Pell, A. J.; Dronskowski, R.; Kustrowski, P.; Slabon, A. Exploring the Origins of Improved Photocurrent by Acidic Treatment for Quaternary Tantalum-Based Oxynitride Photoanodes on the Example of $CaTaO_2N$. *J. Phys. Chem. C* **2020**, *124*, 152–160.
(42) Lin, D.-H.; Chang, K.-S. Photocatalytic and photoelectrochemical performance of Ta_3N_5 microcolumn films fabricated using facile reactive sputtering. *J. Appl. Phys.* **2016**, *120*, 075303.

(43) Dillip, G. R.; Banerjee, A. N.; Anitha, V. C.; Prasad Raju, B. D.; Joo, S. W.; Ki Min, B. Oxygen Vacancy-Induced Structural, Optical, and Enhanced Supercapacitive Performance of Zinc Oxide Anchored Graphitic Carbon Nanofiber Hybrid Electrodes. *ACS Appl. Mater. Interfaces* **2016**, *8*, 5025–5039.
(44) Hojamberdiev, M.; Bekheet, M. F.; Hart, J. N.; Vequizo, J. J. M.; Yamakata, A.; Yubuta, K.; Gurlo, A.; Hasegawa, M.; Domen, K.; Teshima, K. Elucidating the impact of A-site cation change on photocatalytic H_2 and O_2 evolution activities of perovskite-type *Ln*$TaON_2$ (*Ln* = La and Pr). *Phys. Chem. Chem. Phys.* **2017**, *19*, 22210–22220.
(45) Peter, L. M. Dynamic aspects of semiconductor photoelectrochemistry. *Chem. Rev*. **1990**, *90*, 753–769.
(46) Takanabe, K. Photocatalytic Water Splitting: Quantitative Approaches toward Photocatalyst by Design. *ACS Catal.* **2017**, *7*, 8006–8022.
(47) Hojamberdiev, M.; Vargas, R.; Bhati, V. S.; Torres, D.; Kadirova, Z. C.; Kumar, M. Unraveling the photoelectrochemical behavior of Ni-modify ZnO and TiO_2 thin films fabricated by RF magnetron sputtering. *J. Electroanal. Chem.* **2021**, *882*, 115009.
(48) Zeng, L.; Sun, K.; Chen, Y.; Liu, Z.; Chen, Y.; Pan, Y.; Zhao, R.; Liu, Y.; Liu, C. Neutral-pH overall water splitting catalyzed efficiently by a hollow and porous structured ternary nickel sulfoselenide electrocatalyst. *J. Mater. Chem. A* **2019**, *7*, 16793–16802.
(49) Obata, K.; van de Krol, R.; Schwarze, M.; Schomäcker, R.; Abdi, F.F. In situ observation of pH change during water splitting in neutral pH conditions: impact of natural convection driven by buoyancy effects. *Energy Environ. Sci.* **2020**, *13*, 5104–5116.
(50) Obata, K.; Abdi, F. F. Bubble-induced convection stabilizes the local pH during solar water splitting in neutral pH electrolytes. *Sustain. Energ. Fuels* **2021**, *5*, 3791–3801.
(51) Oliva, F. Y.; Avalle, L. B.; Santos, E.; Cámara, O. R. Photoelectrochemical characterization of nanocrystalline TiO_2 films on titanium substrates. *J. Photochem. Photobiol. A* **2002**, *146*, 175–188.
(52) Hojamberdiev, M.; Kawashima, K. Exploring flux-grown transition metal oxynitrides perovskites for photocatalytic water oxidation: A minireview. *Ener. Rep.* **2020**, *6*, 13–24.
(53) Zhang, Q.; Celorio, V.; Bradley, K.; Eisner, F.; Cherns, D.; Yan, E.; Fermín, D. Density of deep trap states in oriented TiO_2 nanotube arrays. *J. Phys. Chem. C* **2014**, *118*, 18207–18213.
(54) Fabregat-Santiago, F.; Garcia-Belmonte, G.; Bisquert, J.; Bogdanoff, P.; Zaban, A. Mott-Schottky analysis of nanoporous semiconductor electrodes in dielectric state deposited on SnO_2(F) conducting substrates. *J. Electrochem. Soc*. **2003**, *150*, E293–E298.
(55) Peter, L.; Walker, A. B.; Bein, T.; Hufnagel, A. G.; Kondofersky, I. Interpretation of photocurrent transients at semiconductor electrodes: effects of band-edge unpinning. *J. Electroanal. Chem.* **2020**, *872*, 114234.
(56) Landsmann, S.; Maegli, A. E.; Trottmann, M.; Battaglia, C.; Weidenkaff, A.; Pokrant, S. Design Guidelines for High-Performance Particle-Based Photoanodes for Water Splitting: Lanthanum Titanium Oxynitride as a Model. *ChemSusChem* **2015**, *8*, 3451–3458.
(57) Osterloh, F. E. Inorganic nanostructures for photoelectrochemical and photocatalytic water splitting. *Chem. Soc. Rev.* **2013**, *42*, 2294–2320.
(58) Bisquert, J.; Zaban, A.; Greenshtein, M.; Mora-Seró, I. Determination of rate constant for charge transfer and distribution of semiconductor and electrolyte electronic energy levels in dye-sensitized solar cells by open-circuit photovoltage decay method. *J. Am. Chem. Soc*. **2004**, *16*, 13550–13559.
(59) Yamakata, A.; Kawaguchi, M.; Nishimura, N.; Minegishi, T.; Kubota, J.; Domen, K. Behavior and Energy States of Photogenerated Charge Carriers on Pt- or CoO_x-Loaded $LaTiO_2N$ Photocatalysts: Time-Resolved Visible to Mid-Infrared Absorption Study. *J. Phys. Chem. C* **2014**, *118*, 23897–23906.

(60) Kawashima, K.; Hojamberdiev, M.; Wagata, H.; Yubuta, K.; Vequizo, J. J. M.; Yamakata, A.; Oishi, S.; Domen, K.; Teshima, K. NH_3-Assisted Flux-Mediated Direct Growth of $LaTiO_2N$ Crystallites for Visible-Light-Induced Water Splitting, *J. Phys. Chem. C* **2015**, *119*, 15896–15904.
(61) Hojamberdiev, M.; Wagata, H.; Yubuta, K.; Kawashima, K.; Vequizo, J. J. M.; Yamakata, A.; Oishi, S.; Domen, K.; Teshima, K. KCl flux-induced growth of isometric crystals of cadmium-containing early transition-metal (Ti^{4+}, Nb^{5+}, and Ta^{5+}) oxides and nitridability to form their (oxy)nitride derivatives under an NH_3 atmosphere for water splitting application. *Appl. Catal. B* **2016**, *182*, 626–635.
(62) Kato, K.; Yamakata, A. Defect-Induced Acceleration and Deceleration of Photocarrier Recombination in $SrTiO_3$ Powders. *J. Phys. Chem. C* **2020**, *124*, 11057–11063.

For Table of Contents Use Only

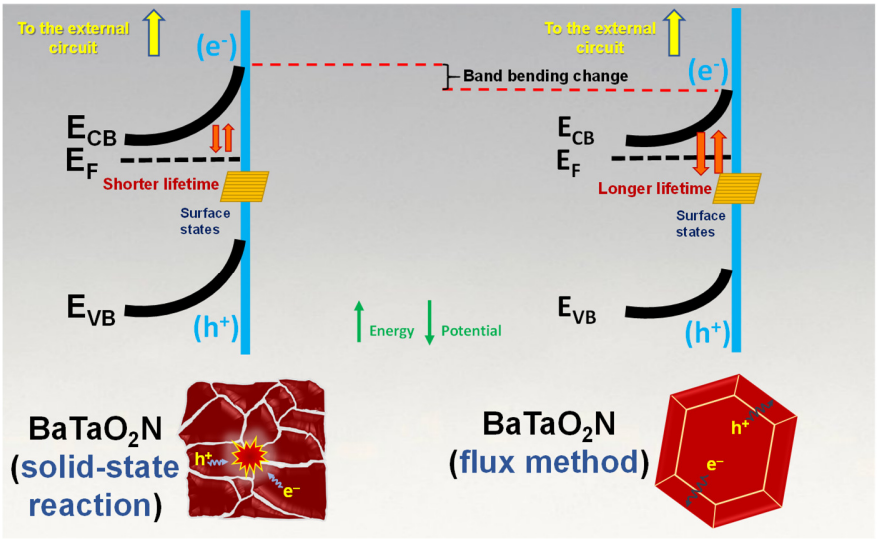

To reduce the synthesis time and defect density of $BaTaO_2N$ by a fresh supply of more active nitriding species and minimizing the generation of N_2 and H_2, an NH_3 delivery system was localized just above the synthesis mixture. $BaTaO_2N$ synthesized by flux method had a greater number of holes for water oxidation reaction compared with $BaTaO_2N$ synthesized by solid-state reaction.